

On the scattering correction of fast-ion D-alpha signals on NSTX-U

G. Z. Hao, W. W. Heidbrink, D. Liu, L. Stagner, M. Podestà, and A. Bortolon

Citation: [Review of Scientific Instruments](#) **89**, 063507 (2018); doi: 10.1063/1.5031879

View online: <https://doi.org/10.1063/1.5031879>

View Table of Contents: <http://aip.scitation.org/toc/rsi/89/6>

Published by the [American Institute of Physics](#)

Articles you may be interested in

[Instrumentation for in situ flow electrochemical Scanning Transmission X-ray Microscopy \(STXM\)](#)

[Review of Scientific Instruments](#) **89**, 063702 (2018); 10.1063/1.5023288

[Immersion-scanning-tunneling-microscope for long-term variable-temperature experiments at liquid-solid interfaces](#)

[Review of Scientific Instruments](#) **89**, 053707 (2018); 10.1063/1.5030407

[Advanced readout methods for superheated emulsion detectors](#)

[Review of Scientific Instruments](#) **89**, 053304 (2018); 10.1063/1.5017756

[Preface: Invited Papers from the 17th Annual International Conference on Ion Sources](#)

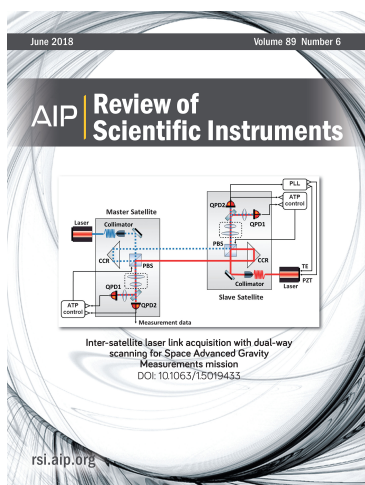
[Review of Scientific Instruments](#) **89**, 051901 (2018); 10.1063/1.5038775

[Note: Optics design of a periscope for the KSTAR visible inspection system with mitigated neutron damages on the camera](#)

[Review of Scientific Instruments](#) **89**, 066102 (2018); 10.1063/1.5033567

[Inter-satellite laser link acquisition with dual-way scanning for Space Advanced Gravity Measurements mission](#)

[Review of Scientific Instruments](#) **89**, 064501 (2018); 10.1063/1.5019433



On the scattering correction of fast-ion D-alpha signals on NSTX-U

G. Z. Hao,^{1,a)} W. W. Heidbrink,¹ D. Liu,¹ L. Stagner,¹ M. Podestà,² and A. Bortolon²

¹University of California, Irvine, California 92697, USA

²Princeton Plasma Physics Laboratory, Princeton, New Jersey 08540, USA

(Received 1 April 2018; accepted 27 May 2018; published online 18 June 2018)

Analysis of fast-ion D-alpha (FIDA) data on National Spherical Torus Experiment-Upgrade (NSTX-U) shows that the cold D_α line contaminates the FIDA baseline. The scattered light is comparable to the FIDA emission. A scattering correction is required to extract the FIDA signal. Two methods that relate the scattered light contamination to the intensity of the cold D_α line are employed. One method uses laboratory measurements with a calibration lamp; the other method uses data acquired during plasma operation and singular value decomposition analysis. After correction, both the FIDA spectra and spatial profile are in better agreement with theoretical predictions. *Published by AIP Publishing.* <https://doi.org/10.1063/1.5031879>

I. INTRODUCTION

In the present magnetically confined fusion devices, the study of fast ion confinement is an important topic since fast ions have significant influence on the plasma heating and current drive. A fast-ion D-alpha (FIDA) diagnostic is an appealing way to obtain information about the fast-ion population. FIDA measures the Doppler-shifted deuterium Balmer alpha line, which is emitted by the fast neutrals that undergo an energy level transition from $n = 3$ to $n = 2$. Here, the fast neutrals come from the charge exchange (CX) recombination process between the fast ions and neutrals; the neutrals can be either injected neutrals or edge neutrals. Edge neutrals are produced by particle recycling between the plasma and vessel wall. Background subtraction is required to extract FIDA emission from the measured signal. The background emission is mainly caused by the visible bremsstrahlung emission, passive FIDA, impurity radiation, and molecular emission.¹⁻³ Here, passive FIDA means the FIDA signal produced by the CX between fast ions and edge neutrals.⁴ However, successful background subtraction is a challenge for the FIDA technique since the FIDA emission is relatively weak and its spectrum is easily contaminated by other light sources, such as the scattered light of the cold D_α (656.1 nm).⁵

In the experiment, there are basically two methods to subtract background emission. One is the beam modulation method, which uses the signal from beam-off phases to determine background emission. When the discharge is stationary, this method works well.^{1,2,6} Another method is to utilize the signal from a toroidally displaced reference view that misses the injected beam. Since the background emission is continually monitored, reference views can provide better temporal resolution than time-slice subtraction. On the other hand, if the background is toroidally asymmetric, time-slice subtraction is preferred. In addition, on other devices such as Axially Symmetric Divertor Experiment Upgrade (ASDEX-U), the background emission can be approximately represented by bremsstrahlung emission, and the bremsstrahlung emission is well simulated² by calculations with the synthetic diagnostic

code FIDASIM.⁷ However, as shown below, this approximation is not available for National Spherical Torus Experiment-Upgrade (NSTX-U) since the modeled bremsstrahlung emission is much smaller than the measured baseline level.

On NSTX-U, the installed vertical (v -) and tangential (t -) FIDA systems are designed to study the perpendicular and parallel dynamics of fast ions, respectively.^{8,9} v -FIDA has operated since 2008, and t -FIDA began to acquire data during the NSTX-U 2016 experimental campaign. Both systems utilize reference views. However, the baseline levels of the paired views of v -FIDA exhibit different time evolution during a discharge,⁸ which implies that the measured signal from the reference view cannot be directly taken as the background emission to subtract from the active-view signal to obtain the net FIDA emission. For the t -FIDA system, the problems are similar. During previous data analysis, a rescaling factor in time was applied to reference-view data to compensate for the discrepancy between the active view and reference view baselines.^{8,10} On the Mega-Ampere Spherical Tokamak (MAST), a similar approach was used to get the net FIDA signal.¹¹ A physically based method of baseline correction should be more accurate than these empirical time-dependent adjustments.

In this study, it is found that the scattered light of cold Balmer D_α makes a significant contribution to the measured baseline. Hence, it is worthwhile to remove scattered light from the raw spectra before extracting the net FIDA signal. The singular value decomposition (SVD) method is used to correct the FIDA raw spectra. The applied correction procedure may also be helpful for the stray light correction in other fields, such as correction of measured images of high-contrast Earth scenes using Moderate Resolution Imaging Spectroradiometer.^{12,13}

The contamination sources for the FIDA background emission are discussed in Sec. II. Section III compares two different methods to remove scattered light from the spectra. Conclusions appear in Sec. IV.

II. CONTAMINATED BACKGROUND ISSUE

This section discusses possible contamination sources for the baseline emission and the FIDA spectra measured on NSTX-U. NSTX-U is a small aspect ratio machine

^{a)}Electronic mail: ghao@pppl.gov

(major/minor radii are 0.95 and 0.65 m, respectively), operating at magnetic field $B_T < 1$ T and current $I_p < 2$ MA with the neutral beam injection power (P_{NBI}) up to 12 MW. In this study, the discussed experiments are in the low-confinement mode, with current $I_p = 0.65\text{--}0.8$ MA and field $B_T = 0.63$ T, line-averaged density $n_e = 1\text{--}4 \times 10^{19} \text{ m}^{-3}$, and $P_{NBI} \leq 1$ MW.

The lines of sight (LOS) of the FIDA diagnostic on NSTX-U are plotted in Fig. 1. A detailed description about the FIDA hardware can be found in Refs. 8 and 9. Figure 1(a) shows that the strike point on the passive plate can be seen by the innermost several fibers of v-FIDA, which can induce signal contamination and result in a discrepancy between the active-view baseline and reference-view baseline. The active and reference views of v-FIDA are not identical, as one follows the beam path and the other is purely radial [Fig. 1(b)]. Consequently, they intersect the divertor at slightly different major radii [Fig. 1(c)], which may enhance the discrepancy between the active and reference signals on the innermost fibers, especially for discharges with an X-point. In this study, the fiber position (e.g., $R = 99$ cm) is defined as the major radius where the LOS intercepts the beam line at the midplane. For t-FIDA, the innermost three fibers can see the center stack, which

can contribute to the contamination of the signal. In addition, there is a small major-radius shift (< 2 cm) between the active view fiber and the corresponding reference view fiber. In this paper, in the shown results, the reference view data are already radially interpolated to the corresponding active view position.

A brief schematic of the v-FIDA system is shown in Fig. 2. The active and reference views that collect the light from the plasma are arranged in two columns on the input slits. The light passes through a bandpass filter, a grating, a filter strip, and lenses before it is acquired by a high quantum efficiency charge coupled device (CCD) camera in 2×16 spectral images. For the v-FIDA system on NSTX-U, smearing is avoided by applying a synchronized chopper to block the input light during the readout of CCD data. Typically, the cold D_α emission is about a thousand times larger than the FIDA emission. Scattering of the D_α light by the optical instruments, such as the grating, filter strip, or lenses, can cause non-negligible contamination of the FIDA spectra. In our study, the scattered light is not induced by the overfilling of the grating since the f-number of the collection optics is well matched to that of the spectrometer. The removal of the filter strip reduces the scattering by $\sim 20\%$ but does not eliminate it entirely.

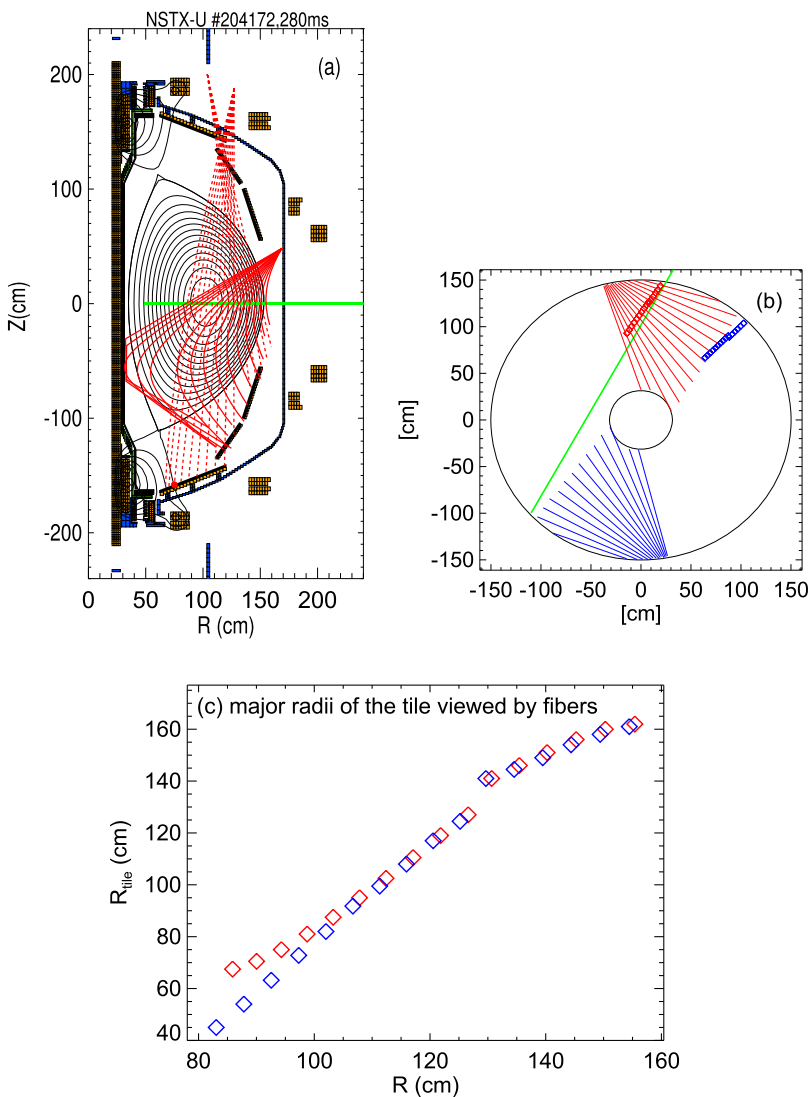


FIG. 1. (a) Elevation and (b) plan view of the LOS of FIDA diagnostics. In (a), dashed and solid curves are the LOS of v/t-FIDA active view, respectively. The red solid point denotes the strike point of the plasma on the passive plate. In (b), symbols denote the v-FIDA LOS, while the solid curves label t-FIDA LOS. Red and blue denote the active view and reference view, respectively. T-FIDA active and reference views are tilted downward (a). The green line shows the centerline of the beam source NBI1C which is used as the diagnostic beam for FIDA spectra in this study. (c) The major radii where active (red) and reference (blue) LOS intercept the vessel versus fiber position for v-FIDA. Here, the fiber position is defined as the major radius where the LOS intercepts the beam line at the midplane. For example, for the fiber at $R = 99$ cm, the major radii where active and reference LOS intercept the divertor are 72.8 and 81 cm, respectively.

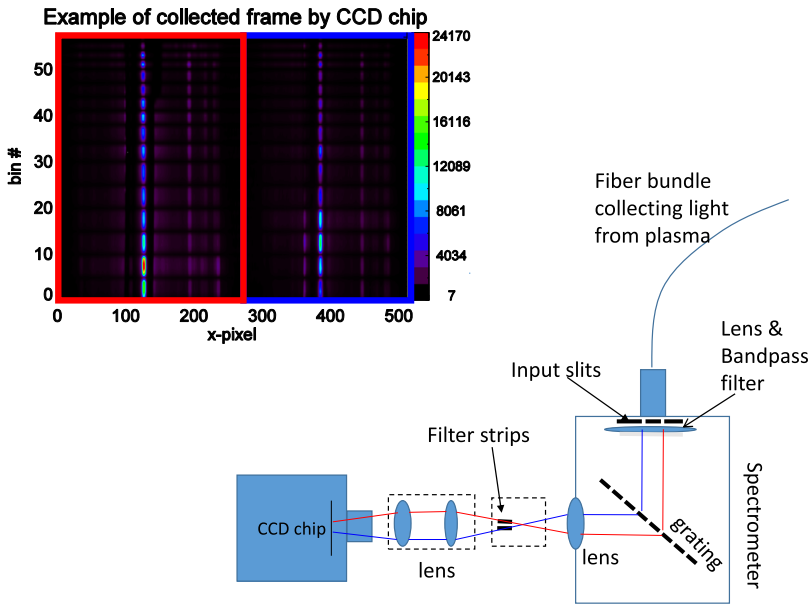


FIG. 2. Brief schematic of the v-FIDA diagnostic. The red and blue lines denote the active-view and reference-view light, respectively. An example of the collected image by the CCD is shown in the inset; the red and blue boxes label the signal from active and reference views, respectively. On the CCD chip, the 2×16 fibers are arranged along the y-axis and rebinned into 58 regions. The spectra are dispersed along the x-pixel. The brightest regions correspond to the attenuated D_α emission.

The bandpass filter excludes wavelengths outside 645–667 nm. Hence, the CCD counts at wavelengths outside the passband (644.3 and 667.1 nm) are expected to be very small and close to zero after removing the vacuum light. Figure 3(a) plots the raw spectra and transmission curves. The measured signals at the boundary pixels ($=0$, and $=255$) are much larger than the expected un-scattered light. For example, at pixel = 0, the measured value 1500 is much larger than the expected un-scattered radiation ~ 250 ($0.05 \times 10^5 \times 5\%$) counts. Hence, the

count at the boundary is dominantly induced by the contamination, although there is very weak radiation from plasma. In Fig. 3(a), the D_α emission is strongly attenuated by the strip made from the neutral material, of which the light transmission rate is 1% in name. In practice, based on the transmission curve of the neutral strip, we can accurately get the intensity of the D_α emission as used in Figs. 3(b) and 3(c). Figures 3(b) and 3(c) demonstrate that the counts at the boundary pixels depend almost linearly on the D_α intensity summed over

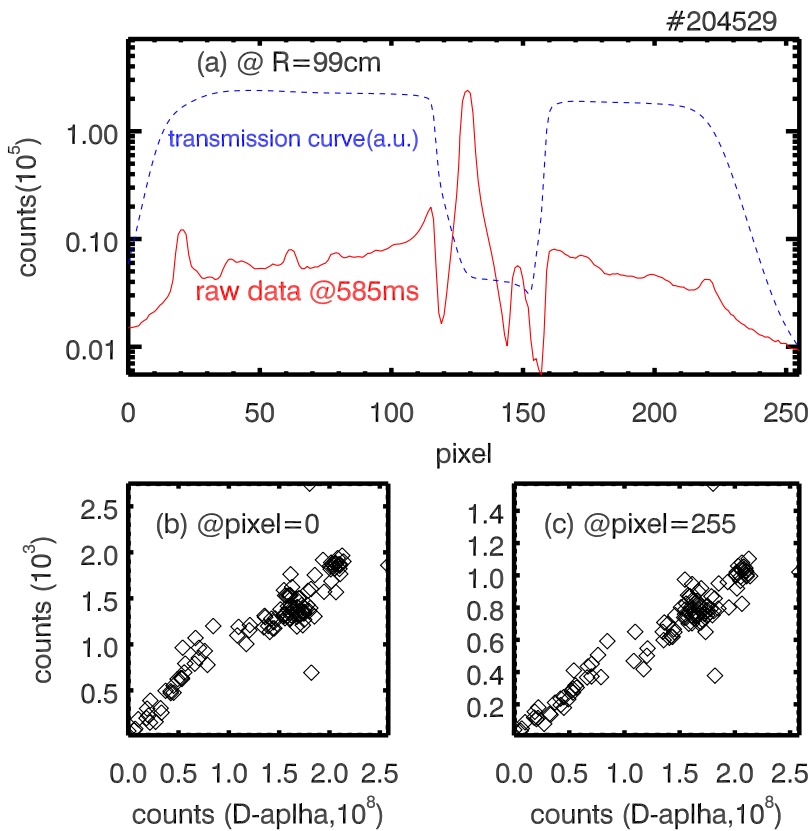


FIG. 3. (a) An example of the transmission curve and the collected signal on the CCD chip for a certain fiber. [(b) and (c)] The counts at boundary pixels as a function of the D_α intensity summed over several dominant fibers, which are the active-view fibers at $R = 94, 99, 103, 108$ cm and the reference-view fibers at $R = 97$ and 102 cm.

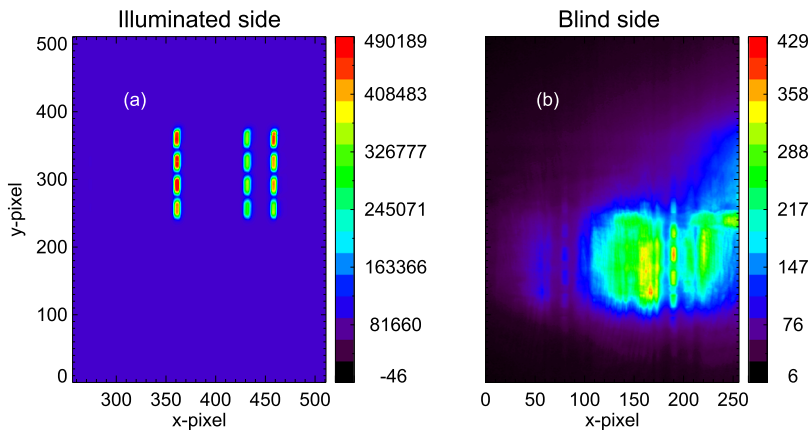


FIG. 4. (a) One half of CCD frame, in which four fibers are illuminated by a neon lamp. (b) Other half of CCD frame, in which no fibers are illuminated. Here, the x-pixel corresponds to the wavelength space.

several dominant fibers. This suggests that scattered D_α light may cause the elevated background.

An initial laboratory test is performed to confirm that scattered light is the correct order of magnitude to explain Fig. 3. An input fiber is connected to a neon lamp rather than the plasma. By design, one half side of the CCD sensor along the x-pixel direction is used to collect the signal from the active-view fibers, which are arranged vertically. The other side is used to collect reference-view data.⁸ The test results are shown in Fig. 4. Scattered or reflected light appears in the blind side of the camera chip, in which no fibers are illuminated. The scattering contamination depends on the wavelength/pixel; hence, the scattered light cannot be modeled by a simple straight line in wavelength space. In addition, the test results show that the scattering contamination level can be $\sim 0.1\%$ of the total input signal for the test case, which is comparable to the ratio of the baseline level to cold D_α radiation on the NSTX-U device.

Consequently, measured baselines during plasma shots often differ between active and reference views. Figure 5 is an example of the Doppler blue-shifted side of v-FIDA measured spectra. The camera exposure time is 10 ms for each time slice, with the light blocked for about 2 ms to avoid smearing

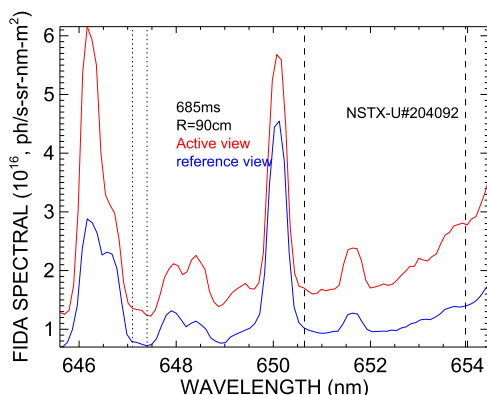


FIG. 5. v-FIDA spectra from active (red) and reference (blue) views. The vertical dotted lines (from 647.1 to 647.4 nm) define the wavelength region used to estimate the baseline radiation. The vertical dashed lines illustrate the wavelength region for FIDA radiation, from 650.64 to 653.96 nm, corresponding to the fast-ion energy component along the LOS (E_i) from 15 to 65 keV.

during the camera readout. In this and the following figures associated with signal time, the middle time (e.g., 685 ms) is used to label the exposure time interval (680–690 ms). Figure 5 shows that there exists a large difference between the active-view baseline and reference-view baseline.

Figure 6 shows the time evolution of the FIDA baseline in a typical L-mode discharge. Figures 6(d) and 6(e) indicate that the measured baselines from active and reference views undergo different evolution for the chosen fibers. For the fiber at R = 99 cm, which can see the divertor region, the active view baseline always increases in the chosen time window; in contrast, the reference view baseline increases from 0.4 to 0.7 s and then has a weak decay from 0.7 to 1.0 s. For the fiber at R = 131 cm, the time evolution of the active and reference view signals are similar; however, the amplitudes are different.

Figures 6(d) and 6(e) also show that the amplitudes of the measured baselines are an order of magnitude larger than the simulated bremsstrahlung emission. In the bremsstrahlung computation, the whole plasma inside the last flux surface is considered. The bremsstrahlung computation uses a 3D simulation grid and time-dependent equilibrium profiles from the TRANSP output. In every simulation cell along the given LOS, the bremsstrahlung emission is computed using the local electron density and temperature. The formula for calculating the bremsstrahlung is¹⁴

$$\frac{dN_{Brems}}{d\lambda} = 7.57 \times 10^{-9} g \frac{n_e^2 Z_{eff}^2}{\lambda T_e^{1/2}} e^{-hc/\lambda T_e}. \quad (1)$$

Here, λ is the wavelength in angstroms. n_e and T_e are the local electron density (cm^{-3}) and temperature (eV) in the simulated cell, respectively. h is the Planck constant. c is the light speed. g is the gaunt factor, which is approximated by $g = 5.542 - (3.108 - \ln(T_e/1000)) (0.6905 - 0.1323/Z_{eff})$. $Z_{eff} = 1.5$ is assumed in the simulation. The total bremsstrahlung emission for each LOS is the integrated N_{Brems} over the intersection length between the LOS and the plasmas.

Uncertainty in Z_{eff} is not enough to explain the discrepancy between the measured baseline and the simulated bremsstrahlung emission. For the inside fiber (e.g., R = 99 cm) that views the divertor region, the discrepancy between the baselines is larger than for the fibers that miss the divertor region (e.g., R = 131 cm). Figure 6 clearly shows that the

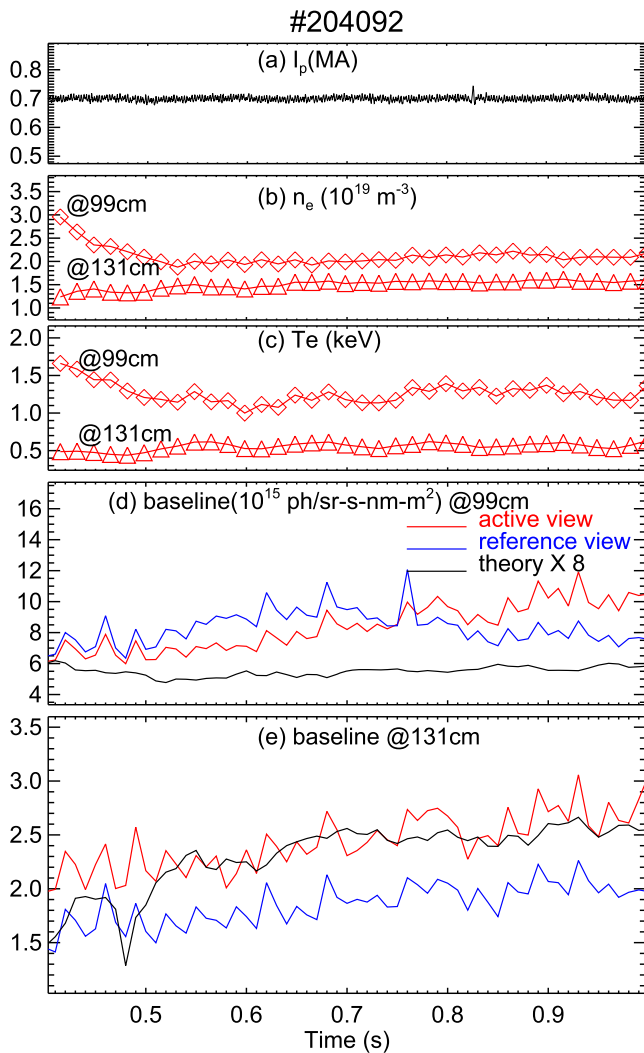


FIG. 6. Time evolution of the measured baseline emission and the bremsstrahlung emission predicted by the FIDASIM code. (a) The plasma current, (b) the electron density at 99 cm and 131 cm, (c) the electron temperature at $R = 99$ and 131 cm, (d) the measured baseline emission from active view and reference view and the FIDASIM computed bremsstrahlung emission at $R = 99$ cm, (e) the baseline and simulated bremsstrahlung emission at $R = 131$ cm.

measured baseline includes additional radiation other than bremsstrahlung.

Next, consider the impact of plasma shape. Figure 7 indicates that the measured baselines on v-FIDA views do not have a clear relation with the evolution of the outer gap for variation between 4 and 11 cm, which implies that the discrepancy between the baselines of the paired views is insensitive to the change in plasma shape. However, Fig. 7(d) shows that t-FIDA seems to come up in 350–400 ms when the outer gap increases. But t-FIDA signals do not decrease later when the gap decreases. The variation of the outer gap can be roughly seen as an indicator of the change in plasma shape. It is suggested that other effects other than the plasma shape play the dominant role for the difference between the baselines of the paired views. In addition, the baseline discrepancy does not have a clear dependence on triangularity and elongation for this shot. Here, we choose a limiter discharge to exclude the

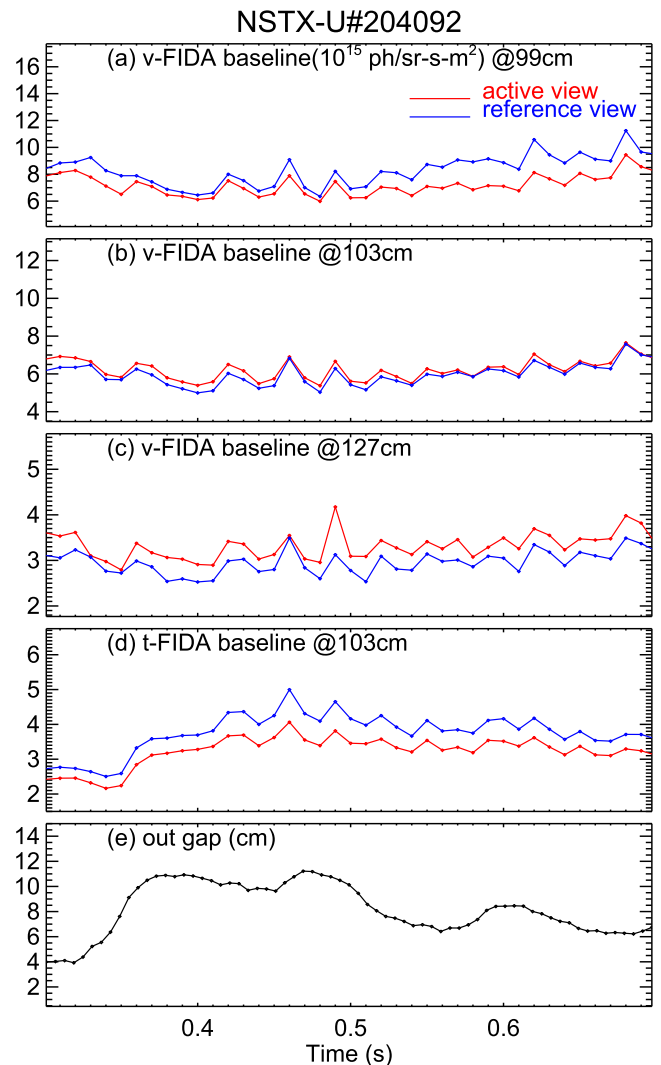


FIG. 7. [(a)–(d)] Time evolution of the measured FIDA baseline and (e) of the outer gap, which is defined as the distance between the last closed flux surface and the limiter on the low-field side.

influence of the x-point and strike point on the measured baseline. A divertor discharge case is shown in Fig. 8.

Figures 8(a) and 8(b) show that, for the v-FIDA fiber at $R = 99$ cm, when the strike point intersects the LOS, the baselines of the active and reference views increase simultaneously, and their discrepancy is significantly enhanced. When the strike point moves outside the LOS, the discrepancy of baselines is reduced; however, the neighboring baseline at $R = 103$ cm is changed significantly by the appearance of the strike point. For the inner v-FIDA fibers, baseline variations are strongly correlated with the strike point position on the passive plate. The LOS of active and reference fibers (e.g., $R = 99$ cm) intersect the divertor region at slightly different major radii [Fig. 1(c)], which is considered the main reason that the discrepancy between active and reference signals on the inner fibers is significantly enhanced when the strike point is near. On the other hand, for the outer v-FIDA fiber at $R = 127$ cm [Fig. 8(d)], which is far away from the strike point during the discharge, the evolution of the baseline does not depend on the strike point position. Similarly, for the t-FIDA fiber at

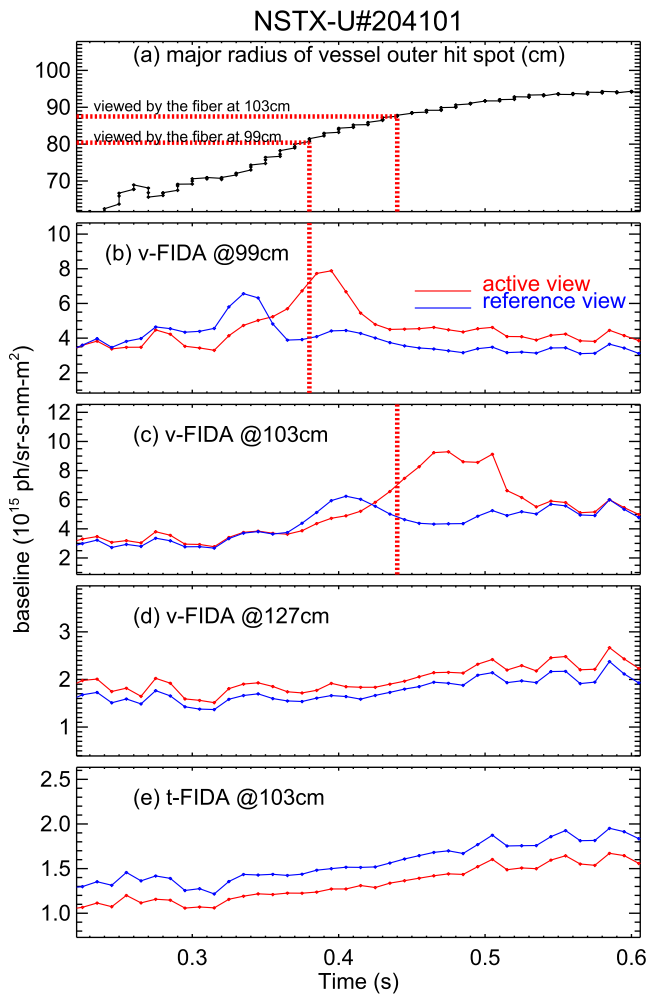


FIG. 8. (a) The major radius of the strike point on the passive plate, which is viewed by several fibers during its variation. The dashed red lines denote two strike positions at its corresponding strike times. [(b)–(e)] Time evolution of the baseline of paired views. The fibers in (b) and (c) view the strike point, while the fibers in (d) and (e) do not. In (b) and (c), the dashed red lines denote the time when the fiber can view the strike point. In (b) and (c), it is worth noting that the major radii where the active and reference views intercept the divertor are different [Fig. 1(c)].

R = 103 cm [Fig. 8(e)], the baseline evolution does not depend on the strike point position. Here, all of the t-FIDA fibers are aligned to avoid viewing the divertor region.⁹ To summarize,

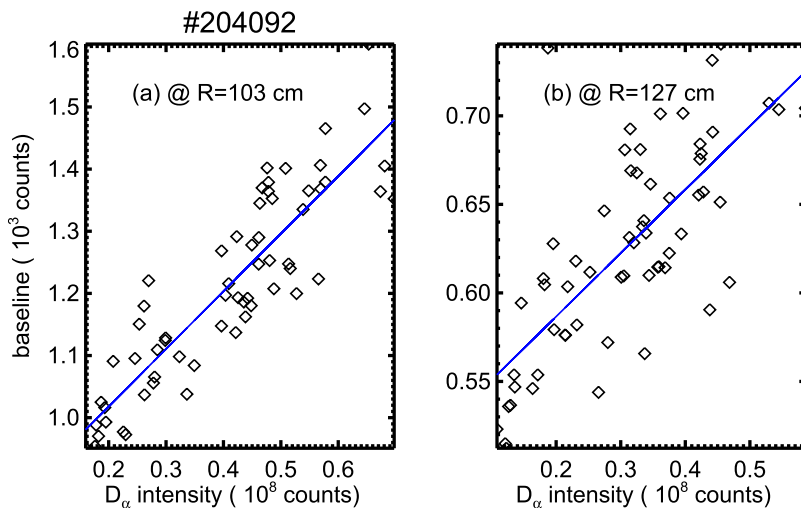


FIG. 9. Baseline of v-FIDA active view at R = 103 cm (a) and R = 127 cm (b) versus the D_α intensity summed over the dominant fibers. The chosen dominant fiber for (a) is the active-view fibers at R = 94 and 99 cm and the reference-view fiber at R = 97 cm. The chosen dominant fiber for (b) is the active-view fiber at R = 99 cm and the reference-view fiber at R = 97 cm. The solid line is the linearly fitted line.

the baseline of fibers that view the divertor depend sensitively on the divertor position, but other views are insensitive.

In Fig. 9, for v-FIDA, the dependence of the baseline on the D_α intensity summed over several dominant fibers is plotted. In the plot, the samples are chosen during the flat-top phase of the plasma current in a limiter discharge. The baseline has a linear dependence on the cold D_α intensity. This dependence is valid for most fibers. Here, the chosen wavelength region (647.1–647.4 nm) for estimating the baseline is about 9 nm away from the cold D_α line (656.1 nm) and the full width at half maximum of the optical instruments is 0.5 nm, so the measured baseline is in the region outside of the wing of the cold D_α line. Hence, the linear correlation between the baseline and the D_α signal suggests that scattering from cold D_α contributes significantly to the baseline signal. The light scattering is different for different fibers.

The FIDA profile based on the raw data before making a scattering correction is shown in Fig. 10. The FIDA signal arises from the charge exchange between the fast ions in the steady state distribution and the injected neutrals. The beam source NBIIC is turned on at 590 ms in this discharge. Since the fast-ion slowing time is on the order of 50 ms, the fast-ion distribution should approach steady state by 650 ms.¹⁵ Here, the major radius of the magnetic axis is at 101 cm based on the EFIT equilibrium reconstruction. Figure 10(b) shows that the level of the scattered light is comparable with the extracted net FIDA signal, which implies that the scattered light can affect the net FIDA signal. Figure 10(c) shows that the inferred FIDA profile has a sharp variation in the region 90–110 cm, and the signal level in the region <90 cm is much larger than that in the region >110 cm. In addition, the counts at fiber R = 100 cm are negative. This profile is unphysical. Moreover, the unphysical profile is reproducibly observed in this discharge (Fig. 10). Scattered light is a likely explanation for the unreasonable FIDA profile. Hence, a scattering correction on the raw FIDA spectrum is required to obtain reasonable FIDA information.

In order to reduce the discrepancy between the active-view baseline and the reference-view baseline and to eliminate the influence of the scattered light on the net FIDA signal, methods are needed to correct the measured raw spectra and then extract

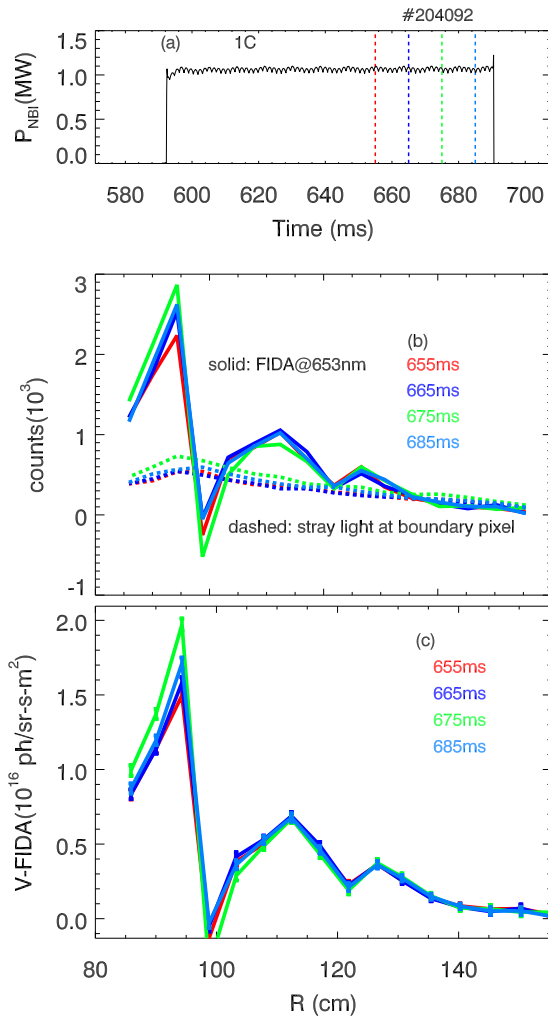


FIG. 10. (a) The waveform of the NBI with the full energy 65 keV; (b) the comparison between the scattered light at the boundary pixels (dashed lines) and the net FIDA signal at 653 nm without a scattering correction (solid lines); (c) the obtained FIDA profile using the raw active signal minus the raw reference signal and integrating between 652.095 and 653.478 nm, corresponding to E_{λ} between 35 and 15 keV. The error bar corresponds to the photon statistics in the FIDA spectra. Colors label the different exposure time intervals.

the net FIDA signal. Two approaches to accomplish this task are presented in Sec. III.

III. SCATTERING COEFFICIENTS

Based on the analysis of Sec. II, we make the following assumptions:

1. Cold D_{α} light is the dominant source of scattered light, as suggested by Fig. 9.
2. An accurate measurement of the cold D_{α} intensity is available for each fiber that is connected to the spectrometer. The measured intensity of the k th fiber $I(k, t)$ depends on the sightline and on the time evolution t of the plasma.
3. The scattering properties of the optical instrument are independent of time, but scattered light can appear anywhere on the chip. Consider a pixel (i, j) , where i represents the row on the chip (corresponding to a particular fiber view) and j represents a horizontal pixel

(corresponding to a particular wavelength) on that row. The scattered light at the (i, j) -th pixel $S(i, j, t)$ is the sum of light scattered from all of the fiber views that are connected to the camera,

$$S(i, j, t) = \sum_{k=1}^{N_f} C(i, j, k) \times I(k, t). \quad (2)$$

Here, N_f is the total number of fibers whose signals are collected by the CCD chip, with $N_f = 32$ for v-FIDA on NSTX-U. The quantity $C(i, j, k)$ is a scattering coefficient that relates D_{α} light from the k th fiber to contamination at the (i, j) -th pixel on the camera.

The goal of this section is to find the scattering coefficients C .

A. Singular value decomposition

The SVD method is already used to perform data analysis in the fusion community,^{16–18} such as for the soft x-ray data analysis to infer the instability mode structure.¹⁹ For the FIDA spectral correction, we assume that the measured total signal $T_A(i, j, t_s)$ for the (i, j) -th pixel in the s th exposure time interval t_s can be written as

$$T_A(i, j, t_s) = P_A(i, j, t_s) + S_A(i, j, t_s) + A(i, j, t_s). \quad (3)$$

Here, $P_A(i, j, t_s)$ is the background signal acquired by the active view fiber, which includes bremsstrahlung emission, impurity lines, passive FIDA, and true cold D_{α} emission without including the instrumental scattering. $S_A(i, j, t_s)$ is the scattered light. $A(i, j, t_s)$ is the FIDA, beam emission, and halo emission associated with active neutral beam injection. Similarly, the measured total signal $T_R(i, j, t_s)$ for a reference view fiber is written as

$$T_R(i, j, t_s) = \epsilon_i P_R(i, j, t_s) + S_R(i, j, t_s), \quad (4)$$

where the subscript “R” denotes the reference view and ϵ_i denotes the collection efficiency of plasma light for the i th view channel, which may differ between the active and reference views. The factor ϵ_i should be a constant in time and is assumed constant for all wavelength pixels j in a given row; ϵ_i is found by measuring the ratio of the oxygen line (650.024 nm) at the active view to that at the reference view in an Ohmic discharge for each channel i . Without auxiliary heating, the oxygen impurity emission should be toroidally symmetric. Note that this method of determining ϵ_i assumes that the oxygen line is much brighter than the scattered light.

The next step is to calculate the scattered component using the SVD method. We choose times during the beam-off phase, in which the FIDA signal $A(i, j, t_s)$ is expected to be zero. The $A(i, j, t_s)$ is written as

$$A(i, j, t_s) = 0 = T_A(i, j, t_s) - P_A(i, j, t_s) - S_A(i, j, t_s). \quad (5)$$

If one assumes that the background light is toroidally symmetric, then $P_A = P_R$ and, through Eq. (4),

$$A(i, j, t_s) = 0 = T_A(i, j, t_s) - \frac{T_R(i, j, t_s)}{\epsilon_i} - [S_A(i, j, t_s) - \frac{S_R(i, j, t_s)}{\epsilon_i}]. \quad (6)$$

$P_A = P_R$ implies that the measured bremsstrahlung at the active view is equal to that at the reference view. The scattered light

at a particular pixel (i, j) can originate anywhere in the optical system. We assume that scattered cold D_α light predominates and measure the intensity of the cold D_α line for each fiber in the entire chip, $I(k, t_s)$. Here, k labels the fiber at which the measured D_α is extracted. Summing the scattered light from each of the N_f fibers, the contribution of scattered light to the net signal at each pixel is $S_A(i, j, t) - \frac{S_R(i, j, t)}{\epsilon_i} = \sum_j C(i, j, k) \times I(k, t)$, where $C(i, j, k)$ is a matrix of scattering coefficients, which represents the dependence of the light contamination at pixel (i, j) on the cold D_α emission from the k th fiber. Substitution into Eq. (6) yields

$$A(i, j, t_s) = 0 = T_A(i, j, t_s) - \frac{T_R(i, j, t_s)}{\epsilon_i} - \sum_{k=1}^{N_f} C(i, j, k) \times I(k, t_s). \quad (7)$$

Since $T_A(i, j, t_s)$, $\frac{T_R(i, j, t_s)}{\epsilon_i}$, and $I(k, t_s)$ are known, we can use the system of equations defined by Eq. (7) for all pixels (i, j) . In practice, $I(k, t_s)$ is the averaged value of the signal in the region of 655.95 and 656.35 nm, which roughly centers on the cold D_α line. To invert Eq. (7), the D_α intensity in the chosen time series, $I(k, t_s)$, is decomposed into a matrix U with dimension $(N_{t_s} < N_f, N_{t_s})$, a singular value diagonal matrix $S(N_f < N_{t_s}, N_f < N_{t_s})$, and a matrix V with dimension $(N_f < N_{t_s}, N_f < N_{t_s})$, as

$$I = USV^T, \quad (8)$$

where the superscript ‘‘T’’ represents the transpose. N_{t_s} denotes the elements of the chosen time series, and $N_f < N_{t_s}$ denotes the smaller of the two quantities. The columns of U and the columns of V are a set of orthonormal vectors, respectively. The D_α line spatial profiles at the time slices in the beam-off phase [i.e., the columns of $I(k, t_s)$] determine the vectors in U and V and the corresponding singular values. According to Eqs. (5) and (8), the scattering coefficient C is calculated by the matrix equation

$$C = I^\dagger (T_A - \frac{T_R}{\epsilon}) = VS^\dagger U^T (T_A - \frac{T_R}{\epsilon}). \quad (9)$$

Here, the superscript \dagger represents the pseudo-inverse of the matrix. When calculating S^\dagger , only several large singular values (generally $>1\%$ of the maximum) are kept, in order to

avoid noise introduced by the small singular values. Finally, the coefficient C is applied to time slices in the beam-on phase to extract the net FIDA signal using the equation

$$A(i, j, t_s) = T_A(i, j, t_s) - \frac{T_R(i, j, t_s)}{\epsilon_i} - \sum_{k=1}^{N_f} C(i, j, k) \times I(k, t_s). \quad (10)$$

In the application presented in this work, except where noted, the correction is carried out on the net (active-reference) FIDA spectra, not on the spectra associated with individual views.

For a boundary pixel, we assume that the CCD counts originate entirely from the scattered light since at the boundary pixel the plasma emission is blocked by the bandpass filter. The scattering coefficient C_b for a boundary pixel is

$$C_b(i, j_b, k) = VS^\dagger U^T S_b(i, j_b, t_s). \quad (11)$$

$S_b(i, j_b, t_s)$ is the CCD counts at the boundary pixel j_b of the i -th fiber in time bin t_s . In Fig. 11, we calculate C_b based on one fiducial shot 204 529 with 1 MW neutral beam injection (NBI) and apply C_b to another 81 fiducial shots. For #204 529, during the calculation of C_b , we keep the relatively large singularity values for S^\dagger , 1.00, 0.17, 0.09, 0.07, 0.05, 0.03, 0.02, and 0.01, which are normalized to the maximum. The figure shows that, after making the scattering correction, the counts at the boundary pixels are almost zero for all fibers with a reasonable standard deviation. Hence, it is demonstrated that the source for the counts at the boundary pixels is scattered light, and the scattering coefficient does not depend on the plasma condition. Similarly, Fig. 11(b) shows the effect of the scattering correction on the baseline. After making the scattering correction, a value near zero is expected for the baseline difference (net baseline) between the paired views. The scattering correction works well for the outer fibers (>110 cm). For the inner fibers, there is a big offset between the corrected net baseline and the zero line, and the standard deviation is larger. The source of this discrepancy is discussed below.

Figure 12 shows an example (#204092) of the comparison between the corrected FIDA spectra and FIDASIM predictions for v-FIDA for an L-mode discharge with 65 keV neutral beam injection. For #204 092, during the calculation

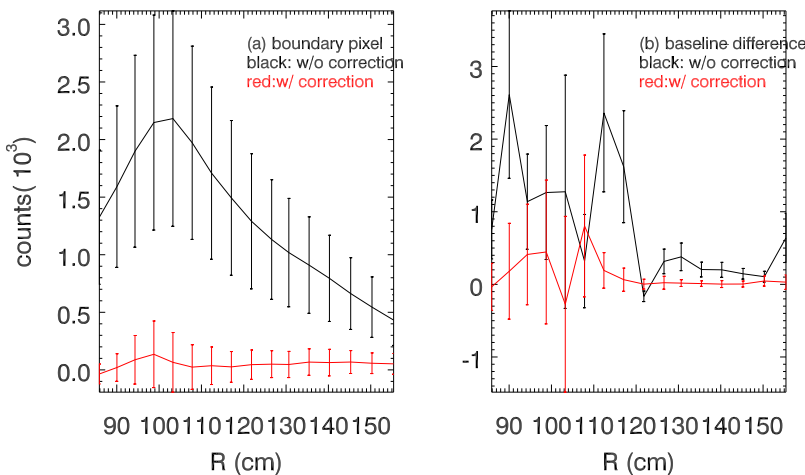


FIG. 11. (a) Comparison between the counts before (black) and after (red) scattering correction. Here, the scattering correction coefficient from fiducial shot 204 529 is applied to 81 fiducial shots. The plotted line is the mean value over 81 fiducial shots, and the error bar is the corresponding standard deviation. (b) The net baseline before (black) and after (red) scattering correction for 81 fiducial shots.

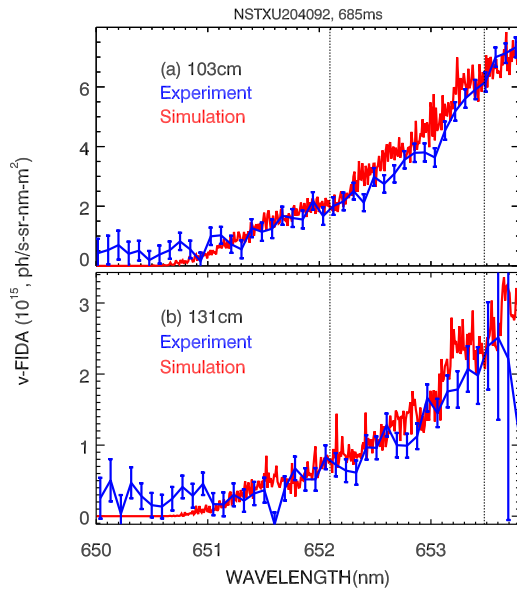


FIG. 12. Comparison between the corrected net FIDA spectra (blue) and the FIDASIM simulation (red) for the fiber at (a) $R = 95$ and (b) 131 cm. The error bars represent the photon statistics and readout noise. The vertical dashed lines denote the wavelength 652.095 nm and 653.478 nm.

of matrix C , we keep the normalized singularity values for S^\dagger : 1.00, 0.22, 0.11, 0.03, 0.02, and 0.01. First, Fig. 12(a) indicates that, as expected, the measured FIDA spectrum is almost zero in the wavelength region below 650.64 nm, which is the possible maximum Doppler shift for a 65 keV deuterium atom. The measured spectra have typical features of a FIDA signal. In addition, both the spectral shape and the absolute amplitude of the experimental spectra are in good agreement with the FIDASIM predictions for the chosen time slice.

Previously, it was reported that NSTX FIDA data are only usable on the blue-shifted side of the spectrum.^{6,8} On the red-shifted side of the spectrum, baseline offsets made the data unusable. With the scattering correction introduced in this section, reasonable baselines are also obtained on the red-shifted sides of the spectrum as shown in Fig. 13.

Figure 14 illustrates that the experimental FIDA profile also agrees well with the simulated profile. Here, the spectra are integrated from 652.095 to 653.478 nm, corresponding to the fast ion energy component along the LOS (E_λ) between 35 and 15 keV, respectively.

However, as shown in Figs. 15(a) and 15(b), the scattering correction fails in some cases. Here, the corrected FIDA spectra are shifted up and down in (a) and (b), respectively; moreover, the corrected experimental baseline is negative in (b), which is unphysical. Figure 15(c) shows the comparison between the experimental FIDA profile and the FIDASIM prediction; in this figure, the offset of the net baseline with respect to zero is included in the experimental error bar. There is poor agreement at the innermost fibers, especially at the fiber $R = 94$ cm. However, examination of many different time slices shows that the correction is robust for fibers at positions larger than 100 cm.

There are two likely reasons that the scattering correction fails for fibers that view the divertor. First, the active

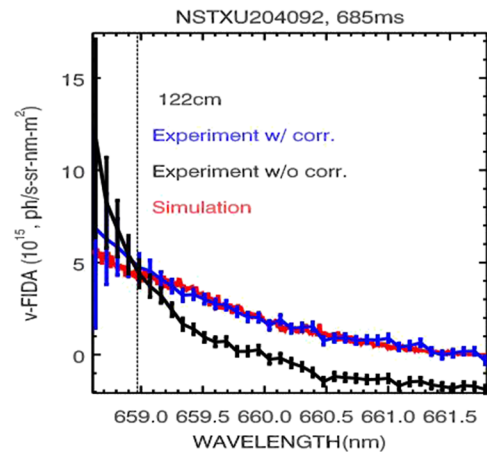


FIG. 13. Experimental spectra with (blue) and without (black) scattering correction and FIDASIM simulated spectra (red) on the red-shifted side of the cold D_α line. The dashed vertical line marks 658.97 nm, corresponding to $E_\lambda = 18$ keV. The large error bars at a small Doppler shift (<658.971 nm) are associated with carbon impurity lines and the coarse boundary of the filter strips.

and reference views intercept the divertor at different radii, which induces a discrepancy between the active and reference signals. The sensitivity of the signal discrepancy on the fiber position is evident in Fig. 8(c). Second, the scattering method [Eq. (5)] assumes that only cold D_α light contributes to the scattering. In the case of a divertor view, scattered impurity or molecular emission may also contribute to the signal.

The scattering correction works best when the SVD correction coefficients C are calculated for the particular plasma conditions under study. The correction of the boundary pixels is insensitive to plasma conditions (Fig. 11), but for FIDA wavelengths, the scattering correction works best if

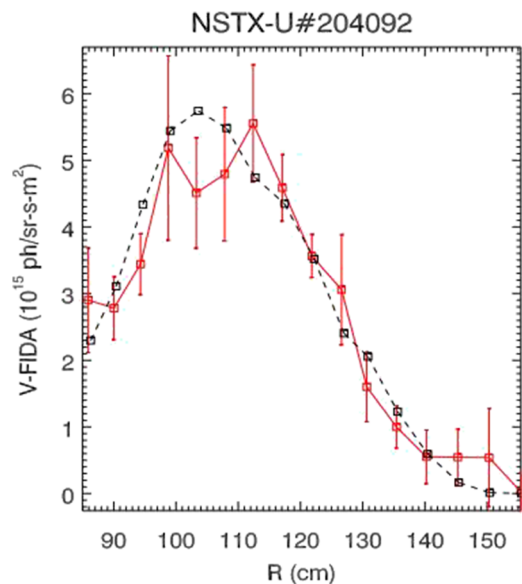


FIG. 14. Comparison between the experimental FIDA profile (red solid curve) and the FIDASIM simulation result (black dashed curve) for 685 ms. Here, the error bars include the offset of the net baseline with respect to zero.

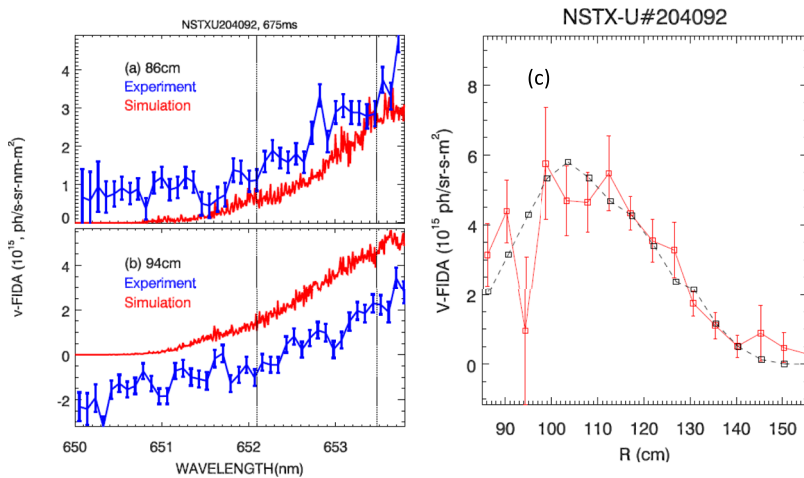


FIG. 15. Comparison between the corrected FIDA spectrum and FIDASIM simulation for v-FIDA fibers at (a) 86 cm and (b) 94 cm. (c) Comparison between the experimental FIDA profile and the FIDASIM simulation. Here, the error bars include the offset of the net baseline with respect to zero.

the coefficients are calculated for the actual discharge conditions during a beam-off period. Apparently, changes in the spatial distribution or spectral content of background light emitted by the plasma alter the optimal scattering coefficients.

B. D_α lamp

In principle, the best way to determine the scattering coefficients is to illuminate individually each fiber with a known source $I(k)$ that matches the cold D_α spectrum emitted by the plasma. In that case, Eq. (2) reduces to $S(i, j) = C(i, j, k)I(k)$ and the desired scattering coefficient for the (i, j) -th pixel is $C(i, j, k) = S(i, j)/I(k)$, where $S(i, j)$ is the signal measured during illumination. In our laboratory test, light from a commercial lamp was bandpass filtered and then connected to each of the input fibers. Unfortunately, even after filtering, the commercial lamp includes appreciable molecular emission in some of the spectral regions of interest. The results presented below are for uncontaminated wavelengths.

Figure 16(a) shows a camera frame when a single fiber is illuminated. The bright stripe in the upper left is the D_α line from the illuminated fiber. In the blind side of the CCD chip, where no fiber is illuminated, there exists scattered light as shown in Fig. 16(b). Attenuation by the neutral filter causes the dark vertical band around pixel 400, showing that at least some of the scattering occurs upstream of the filter strip. It

shows that the reflection contributes the contamination. Tests show that, as expected, the amplitude of the scattered light is linearly proportional to the intensity of input light, while its shape is independent of the intensity.

By illuminating each fiber individually and acquiring data similar to that shown in Fig. 16, scattering coefficients are obtained for all pixels that are uncontaminated by molecular emission. To compare with the SVD method, we select a special central pixel that corresponds to a wavelength that is blocked by the input bandpass filter, so only scattered light is possible. Figure 17(a) compares the coefficients obtained with the lamp and by SVD for this special pixel as a function of illuminated fiber. If the hypothesis that scattered cold D_α light is the dominant source of contamination in the FIDA system is true, the scattering coefficients for the two methods should be of comparable magnitude as observed. Because the lamp intensity is ~ 500 times weaker than the plasma D_α light [Fig. 17(d)], the uncertainty in $C(i, j, k)$ is large when using the lamp, but within the uncertainties, the two methods are consistent.

In practice, both methods are useful but neither works perfectly. Figure 18 compares the time evolution of corrected signals using the two methods for a pixel that should see zero signal. Use of either method is a significant improvement over the uncorrected method. For a central sightline (Fig. 18), the two methods are in excellent agreement with each other and with the true value of zero. However, for other sightlines or cases, the agreement is not always good.

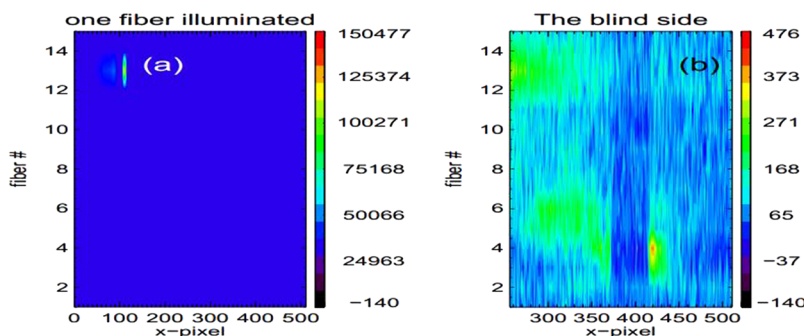


FIG. 16. (a) Obtained CCD whole frame in the on-bench test when one fiber is illuminated. (b) The contamination on the blind side of the CCD chip.

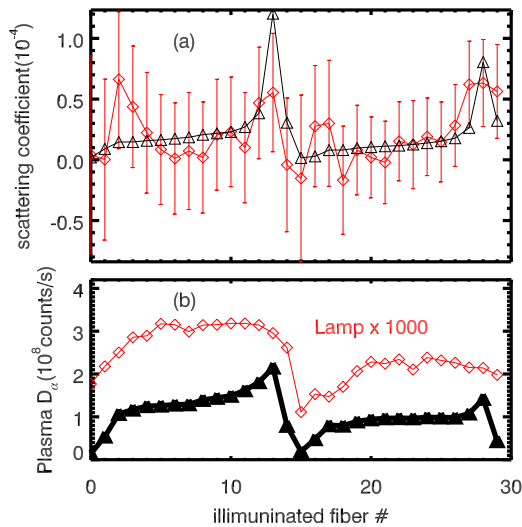


FIG. 17. (a) Comparison of the scattering coefficient $C_b(13, 255, *)$ for the boundary pixel vs. illuminated fiber as determined with a D_α lamp in the laboratory (\diamond) and through the SVD analysis of plasma discharges (\triangle). (b) Comparison of the average cold D_α light that was employed in the SVD analysis with the measured intensity of the D_α lamp (multiplied by 1000) vs. fiber. Fibers 0-14 denote active views; fibers 15-29 denote reference views.

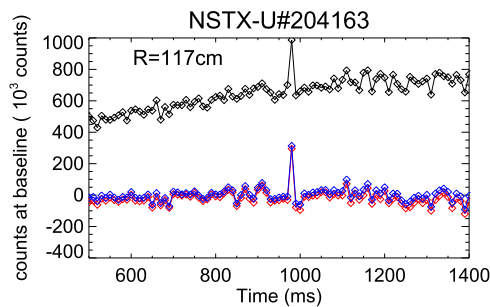


FIG. 18. Time evolution of the measured (black) net baseline, corrected ones using SVD (based on fiducial shot 204 529, blue), and D_α lamp (red) for the fiber at $R = 117$ cm. Here, the net baseline value is estimated by the difference of the measured baseline at the active and reference views. The baseline is defined as the mean counts in the wavelength range 661.5-661.8 nm in the red-shift side.

IV. CONCLUSION

In summary, scattered light contaminates the raw FIDA data on NSTX-U. Pixels that should be dark measure non-zero signals when the fibers are illuminated by a neon or D_α lamp; similarly, during plasma operation, wavelengths that should be blocked by a bandpass filter measure signals that scale linearly with the cold D_α intensity. Owing to the scattered light, baseline shifts are often observed. A method to correct each camera pixel for scattered D_α light is introduced. The method employs measurements of the D_α emission from every sightline together with scattering coefficients derived either from lab measurements with a calibration source or plasma discharges when the active beam is off. Both methods of deriving the scattering coefficients often produce corrected signals with reasonable baselines. After correction, in most cases, the measured vertical FIDA spectra are consistent with FIDASIM predictions in amplitude, spectral shape, and profile shape.

However, the correction often fails for the innermost vertical fibers and the three innermost tangential fibers that view the center stack. For the SVD method, coefficients derived in one discharge can give imperfect correction in a discharge with a different shape. Similarly, at wavelengths where no net signal is expected, the scattering coefficients obtained with the D_α lamp sometimes fail to null the baseline. Reexamining the assumptions of the analysis given at the beginning of Sec. III, a likely explanation for these difficulties is that the actual contaminating light emitted from the plasma is not linearly proportional to the measured D_α intensity at all wavelengths. In the case of the D_α lamp, the lamp's spectrum is not identical to the spectrum emitted by the plasma. For the SVD method, all light emitted by the plasma affects the inferred scattering coefficients, so it is not surprising that the derived coefficients are sensitive to plasma shape since spatial shifts of molecular emission or D_α light that is reflected in the vessel can alter the inferred coefficients. In practice, we calculate the scattering coefficients from both methods and utilize the method that yields baselines that are closest to zero in portions of the spectrum where no net signal is expected. Residual offsets provide an estimate of the error associated with background subtraction.

An ideal FIDA diagnostic would block the cold D_α light before it contaminated the spectra with, for example, a narrow-band notch filter at the entrance to the spectrometer. But, in a system with scattered light, the presented scattering correction significantly improves the reliability of the FIDA data.

ACKNOWLEDGMENTS

We thank Dr. R. Bell for useful discussions on the spectral analysis and the entire NSTX-U team for their support. We also thank the anonymous referees for many helpful suggestions. This work was supported by the US DOE under Grant Nos. DE-AC02-09CH11466, DE-FG02-06ER54867, and DE-FG03-02ER54681.

- ¹Y. Luo, W. W. Heidbrink, K. H. Burrell, D. H. Kaplan, and P. Gohil, "Measurement of the D-alpha spectrum produced by fast ions in DIII-D," *Rev. Sci. Instrum.* **78**(3), 033505 (2007).
- ²B. Geiger, M. Garcia-Munoz, W. W. Heidbrink, R. M. McDermott, G. Tardini, R. Dux, R. Fischer, V. Igocine, and ASDEX Upgrade Team, "Fast-ion D-alpha measurements at ASDEX Upgrade," *Plasma Phys. Controlled Fusion* **53**(6), 065010 (2011).
- ³C. A. Michael, N. Conway, B. Crowley, O. Jones, W. W. Heidbrink, S. Pinches, E. Braeken, R. Akers, C. Challis, M. Turnyanskiy, A. Patel, D. Muir, R. Gaffka, and S. Bailey, "Dual view FIDA measurements on MAST," *Plasma Phys. Controlled Fusion* **55**(9), 095007 (2013).
- ⁴N. G. Bolte, W. W. Heidbrink, D. Pace, M. V. Zeeland, and X. Chen, "Measurement and simulation of passive fast-ion D-alpha emission from the DIII-D tokamak," *Nucl. Fusion* **56**(11), 112023 (2016).
- ⁵C. M. Muscatello, "Velocity-space resolved fast-ion measurements in the DIII-D tokamak," Ph.D. thesis (University of California, Irvine, 2012).
- ⁶W. W. Heidbrink, A. Bortolon, C. M. Muscatello, E. Ruskov, B. A. Grierson, and M. Podesta, "Calibration techniques for fast-ion D-alpha diagnostics," *Rev. Sci. Instrum.* **83**(10), 10D903 (2012).
- ⁷W. W. Heidbrink, D. Liu, Y. Luo, E. Ruskov, and B. Geiger, "A code that simulates fast-ion D_α and neutral particle measurements," *Commun. Comput. Phys.* **10**, 716-741 (2011).
- ⁸M. Podesta, W. W. Heidbrink, R. E. Bell, and R. Feder, "The NSTX fast-ion D-alpha diagnostic," *Rev. Sci. Instrum.* **79**(10), 10E521 (2008).

- ⁹A. Bortolon, W. W. Heidbrink, and M. Podesta, "A tangentially viewing fast ion D-alpha diagnostic for NSTX," *Rev. Sci. Instrum.* **81**(10), 10D728 (2010).
- ¹⁰W. W. Heidbrink, E. Ruskov, D. Liu, L. Stagner, E. D. Fredrickson, M. Podesta, and A. Bortolon, "Analysis of fast-ion D α data from the national spherical torus experiment," *Nucl. Fusion* **56**(5), 056005 (2016).
- ¹¹O. M. Jones, "Experimental fast-ion transport studies on the Mega-Amp Spherical Tokamak," Ph.D. thesis (Durham University, 2015).
- ¹²S. Qiu, G. Godden, X. Wang, and B. Guenther, "Satellite-earth remote sensor scatter effects on earth scene radiometric accuracy," *Metrologia* **37**(5), 411 (2000).
- ¹³W. W. Gregg, "Initial analysis of ocean color data from the ocean color and temperature scanner. I. Imagery analysis," *Appl. Opt.* **38**(3), 476-485 (1999).
- ¹⁴M. A. Van Zeeland, J. H. Yu, N. H. Brooks, W. W. Heidbrink, K. H. Burrell, R. J. Groebner, A. W. Hyatt, T. C. Luce, N. Pablant, W. M. Solomon, and M. R. Wade, "Active and passive spectroscopic imaging in the DIII-D tokamak," *Plasma Phys. Controlled Fusion* **52**(4), 045006 (2010).
- ¹⁵D. Liu, W. W. Heidbrink, D. S. Darrow, S. S. Medley, and A. L. Roquemore, "Study of beam-ion confinement in MHD-quiescent NSTX plasmas," in APS Meeting Abstracts, October 2006.
- ¹⁶T. Dudok de Witt, "Enhancement of multichannel data in plasma physics by biorthogonal decomposition," *Plasma Phys. Controlled Fusion* **37**(2), 117 (1995).
- ¹⁷D. Vezinet, D. Mazon, R. Guirlet, J. Decker, and Y. Peysson, "Impurity density derivation from bandpass soft x-ray tomography: Applicability, perspectives and limitations," *Nucl. Fusion* **54**(8), 083011 (2014).
- ¹⁸E. J. Strait, J. D. King, J. M. Hanson, and N. C. Logan, "Spatial and temporal analysis of DIII-D 3D magnetic diagnostic data," *Rev. Sci. Instrum.* **87**(11), 11D423 (2016).
- ¹⁹D. Li, Y. Liu, J. Svensson, Y. Q. Liu, X. M. Song, L. M. Yu, R. Mao, B. Z. Fu, W. Deng, B. S. Yuan, X. Q. Ji, Y. Xu, W. Chen, Y. Zhou, Q. W. Yang, X. R. Duan, Y. Liu, and HL-2A Team, "Bayesian soft x-ray tomography and MHD mode analysis on HL-2A," *Nucl. Fusion* **56**(3), 036012 (2016).